

Sub-Sharvin conductance and Josephson effect in graphene

Adam Rycerz*

Institute for Theoretical Physics, Jagiellonian University, Łojasiewicza 11, PL-30348 Kraków, Poland

(Dated: February 26, 2026)

Titov and Beenakker [Phys. Rev. B **74**, 041401(R) (2006)] found, by solving the Dirac-Bogoliubov-DeGennes equation, that the product of critical current and normal-state resistance for superconductor-graphene-superconductor (S-g-S) Josephson junction takes values (for a short junction and zero temperature) between $I_c R_N \approx 2.1$ and $I_c R_N \approx 2.4$ in units of e/Δ_0 , where Δ_0 is the superconducting gap. These values are notably higher than the tunnelling bound ($\pi/2$), but lower than the ballistic bound (π). Here we analyze numerically the tunneling of Cooper pairs through S-g-S junctions in which the longitudinal electrostatic potential profile is tuned, within gates electrodes, from a rectangular to a parabolic one. In the unipolar regime (i.e., when the chemical potential is above the top of a barrier, $\mu > 0$), it is found that $I_c R_N$ gradually evolves from the graphene-specific to the ballistic value. At the same time, the normal-state conductance increases from the sub-Sharvin value of $1/R_N \approx (\pi/4) G_{\text{Sharvin}}$ towards the Sharvin value $G_{\text{Sharvin}} = g_0 |\mu| W / (\pi \hbar v_F)$, with the conductance quantum $g_0 = 4e^2/h$, the junction width W , and the Fermi velocity in graphene v_F . In contrast, in the tripolar regime ($\mu < 0$), both normal-state conductance and the critical current are suppressed when smoothing the potential; however, $I_c R_N$ remains close to the graphene-specific range, even for a parabolic potential. The skewness of the current-phase relation is also discussed.

I. INTRODUCTION

Soon after the theoretical prediction [1] and experimental confirmation [2–4] of the Josephson effect, a current-bias Josephson tunnel junction was used to demonstrate that a macroscopic variable, namely the phase difference across a junction, follows the rules of quantum mechanics [5, 6]. Since early 2000s, superconducting circuits containing Josephson junctions are often regarded as the most promising condensed-matter platform for multiqubit quantum information processing [7, 8]. Both the tunneling- [3] and weak-link [4] Josephson junctions offers possibility to control the system parameters by a bias current or magnetic field [9]. However, a control via the electrostatic field effect, commonly used in semiconductor-based devices, is widely-considered as far more versatile and practical [10–14]. In particular, two superconductors separated by a two-dimensional system, such as a semiconducting heterostructure [10], thin Au film [11], or graphene [12], allow one to modify the critical current (I_c) electrostatically, using gate electrode. From a physical perspective, such Josephson-Field-Effect-Transistors operate since—in the short-junction limit—the product $I_c R_N$ (where R_N denotes the resistance of the junction in the normal state) saturates at a value of order Δ_0/e determined by the excitation gap Δ_0 in the superconductors (with a geometry-dependent prefactor) [15–17]. Therefore, the electrostatic control over R_N implies analogous control over I_c .

For a superconductor-graphene-superconductor (S-g-S) Josephson junction, it was shown that the dimensionless prefactor relating $I_c R_N$ and Δ_0/e varies within the range of 2.1 – 2.4 [16–19]. This range is significantly narrower than that allowed for generic mesoscopic Josephson junctions at

zero temperature [15, 20, 21], i.e.,

$$\frac{\pi}{2} \leq I_c R_N \left(\frac{e}{\Delta_0} \right) \leq \pi, \quad (1)$$

where the lower (upper) bound corresponds to the tunneling (ballistic) limit. What is more, the current-phase relation for S-g-S Josephson junction is forward skewed with respect to the familiar sinusoidal behavior [18, 19], and the quantity

$$S = \frac{2\theta_c}{\pi} - 1, \quad (2)$$

where θ_c is the phase difference corresponding to the maximum current (I_c), varies from $S \approx 0.25$ to $S \approx 0.42$, comparing to the range of $0 \leq S \leq 1$ for generic mesoscopic Josephson junctions.

In this paper, we investigate numerically how the critical current and skewness of the current-phase relation for S-g-S Josephson junction behave as functions of doping, supposing that the electrostatic potential barrier is smooth (i.e., potential varies slowly on the scale of atomic separation). Similar problems were addressed previously [16, 17], but here we focus on the effects of the potential profile, which is gradually tuned from a parabolic to a rectangular shape (see Fig. 1), on the selected measurable quantities. Thus, the paper complements recent studies on the normal metal-graphene-normal metal (N-g-N) setup [22–24], in which analogous effects of smooth barriers on conductance, shot noise power, and thermoelectric properties were discussed.

We notice that the effects of time-dependent fields, including Josephson quantum pumping, are beyond the scope of this work [25].

The paper is organized as follows. In Sec. II we present the details of our numerical approach. The key results for a rectangular barrier are summarized in Sec. III. Central results of the paper, concerning the normal-state conductance, the critical current and skewness of the current-phase relation for smooth potentials, are presented in Sec. IV. The conclusions are given in Sec. V.

*Correspondence: rycerz@th.if.uj.edu.pl.

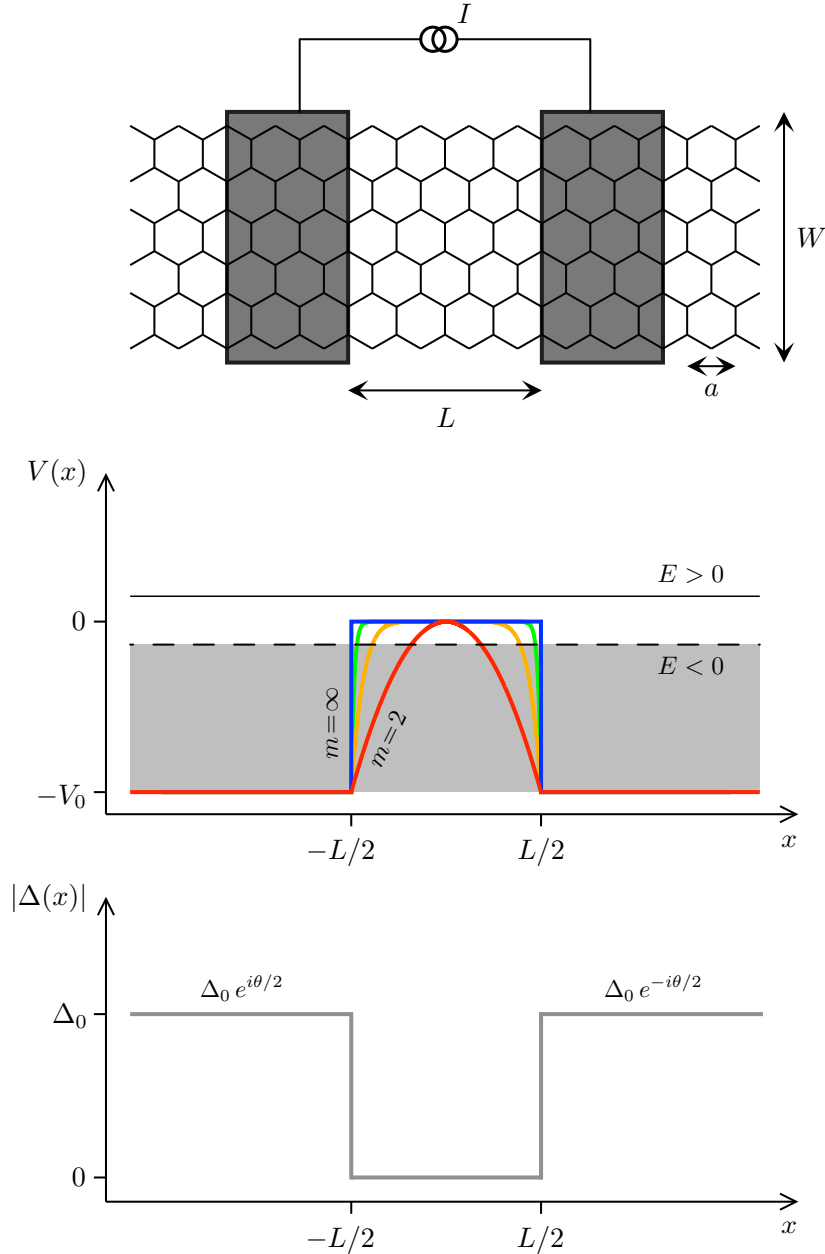


Figure 1: Top: Schematic of a graphene strip of width W , contacted by two superconducting electrodes (dark areas) at a distance L . A current source drives a dissipationless supercurrent through the central region. A separate gate electrode (not shown) allows us to tune the carrier concentration around the neutrality point. The lattice parameter $a = 0.246$ nm is also shown. Middle: Electrostatic potential profiles given by Eq. (5) with $m = 2, 8, 32$, and $m = \infty$ (i.e., the rectangular barrier). The Fermi energy E is defined with respect to the top of a barrier. $E > 0$ corresponds to unipolar n-n-n doping in the device; for $E < 0$, a tripolar n-p-n structure is formed. Bottom: Absolute value of the pair potential with the superconducting phases $\theta/2$ for $x < -L/2$ (left electrode) and $-\theta/2$ for $x > L/2$ (right electrode).

II. MODEL AND METHODS

We start from the Dirac-Bogoliubov-De-Gennes (DBdG) for the system shown schematically in Fig. 1 [16, 17],

$$\begin{pmatrix} \mathcal{H}_0 - \mu & \Delta \\ \Delta^* & \mu - \overline{\mathcal{H}}_0 \end{pmatrix} \begin{pmatrix} \Psi_e \\ \Psi_h \end{pmatrix} = \varepsilon \begin{pmatrix} \Psi_e \\ \Psi_h \end{pmatrix}. \quad (3)$$

Here $\mathcal{H}_0 = v_F \mathbf{p} \cdot \boldsymbol{\sigma} + V(x)$ is the Dirac Hamiltonian for K valley, with $v_F = \sqrt{3} t_0 a / (2\hbar) \approx 10^6$ m/s the energy-independent Fermi velocity in graphene ($t_0 = 2.7$ eV is the nearest-neighbor hopping integral and $a = 0.246$ is the lattice parameter), $\mathbf{p} = (p_x, p_y)$ the in-plane momentum operator (with $p_j = -i\hbar\partial_j$), $\boldsymbol{\sigma} = (\sigma_x, \sigma_y)$ (with σ_j being the Pauli matrices), Ψ_e and Ψ_h are the electron and hole wave functions, $\varepsilon > 0$ is the excitation energy, and μ is the chemical potential (hereinafter, $\mu = E$ — the Fermi energy — since

the $T = 0$ case is considered) in the normal region measured with respect to the Dirac point, so that $\mu = 0$ corresponds to undoped graphene. In the absence of a magnetic field, the Hamiltonian is time-reversal invariant, $\overline{\mathcal{H}}_0 = \mathcal{T}\mathcal{H}_0\mathcal{T}^{-1} = \mathcal{H}_0$, with \mathcal{T} the time-reversal operator [26].

The complex pair potential Δ depends only the position along the strip (x), and can be truncated by adopting the step-function model for the two interfaces between normal region and superconductors at $x = -L/2$ and $x = L/2$, namely

$$\Delta(x) = \begin{cases} \Delta_0 e^{i\theta/2} & \text{if } x < -L/2, \\ 0 & \text{if } |x| \leq L/2, \\ \Delta_0 e^{-i\theta/2} & \text{if } x > L/2, \end{cases} \quad (4)$$

with the bulk superconducting gap Δ_0 and the phase difference between the superconductors θ .

The electrostatic potential energy is chosen as

$$V(x) = -V_0 \times \begin{cases} 1 & \text{if } |x| > L/2, \\ |2x/L|^m & \text{if } |x| \leq L/2, \end{cases} \quad (5)$$

such that changing the value of m tunes the potential from a parabolic shape ($m = 2$) to rectangular shape ($m = \infty$). The potential $V(x)$ is therefore continuous and constant in the leads ($x < -L/2$ or $x > L/2$).

It was shown in Refs. [16, 17] by analysing the spectrum of Andreev states for $\varepsilon < \Delta_0$ that for the short-junction limit, i.e., $L \ll \xi_0$ (with the superconducting coherence length $\xi_0 = \hbar v_F / \Delta_0$; for instance, $\xi_0 \approx 550$ nm for superconducting electrodes made with molybdenum rhenium [19]), the Josephson current can be written as

$$I(\theta) = \frac{e\Delta_0}{\hbar} \sum_{n=0}^{N-1} \frac{T_n \sin \theta}{\sqrt{1 - T_n \sin^2(\theta/2)}}, \quad (6)$$

while the normal-state resistance is given by

$$R_N^{-1} = \frac{4e^2}{h} \sum_{n=0}^{N-1} T_n. \quad (7)$$

In effect, both quantities are determined by the transmission probabilities T_n characterising a graphene strip between two electrodes in the normal state ($\Delta_0 = 0$). Eqs. (6) and (7) coincide, respectively, with the multichannel mesoscopic Josephson equation [15] and the Landauer-Büttiker formula [28]; both formulas are multiplied by a factor of two due to the additional (valley) degeneracy in graphene.

The transmission probabilities in Eqs. (6) and (7), each of which is attributed to the n -th normal mode, with the transverse momentum $k + y = k_y^{(n)} = \pi(n + \frac{1}{2})/W$ (we assume the infinite-mass boundary conditions, see Ref. [27]), can be found by solving the scattering problem for the Dirac equation $\mathcal{H}_0\Psi = E\Psi$. Taking the wave function in a form $\Psi = \phi(x)e^{ik_y y}$, with $\phi(x) = (\phi_a, \phi_b)^T$, one obtains for the central region ($|x| < L/2$)

$$\phi'_a = k_y \phi_a + i \frac{E - V(x)}{\hbar v_F} \phi_b, \quad (8)$$

$$\phi'_b = i \frac{E - V(x)}{\hbar v_F} \phi_a - k_y \phi_b. \quad (9)$$

For the leads ($|x| > L/2$), we have a constant $V(x) = -V_0$, and the solutions can be found analytically, for $E > -V_0$,

$$\phi^{(+)} = \begin{pmatrix} 1 \\ e^{i\vartheta} \end{pmatrix} e^{iK_x x}, \quad \phi^{(-)} = \begin{pmatrix} 1 \\ -e^{-i\vartheta} \end{pmatrix} e^{-iK_x x}, \quad (10)$$

where $e^{i\vartheta} = (K_x + ik_y)/K$, $K = (E + V_0)/\hbar v_F$, and $K_x = \sqrt{K^2 - k_y^2}$. The solutions $\phi^{(+)}$ and $\phi^{(-)}$ represent the propagating waves going to the left and to the right (respectively). The number solutions (for one direction of propagation) is given by

$$N = \lfloor WK/\pi \rfloor. \quad (11)$$

The mode-matching conditions for the interfaces at $x = -L/2$ and $x = L/2$ brought us to the linear system of equations (for a given E and k_y) [22]

$$\begin{bmatrix} \phi_a^{(-)}(x_1) & -\phi_a^{(1)}(x_1) & -\phi_a^{(2)}(x_1) & 0 \\ \phi_b^{(-)}(x_1) & -\phi_b^{(1)}(x_1) & -\phi_b^{(2)}(x_1) & 0 \\ 0 & -\phi_a^{(1)}(x_2) & -\phi_a^{(2)}(x_2) & \phi_a^{(+)}(x_2) \\ 0 & -\phi_b^{(1)}(x_2) & -\phi_b^{(2)}(x_2) & \phi_b^{(+)}(x_2) \end{bmatrix} \begin{bmatrix} r \\ A \\ B \\ t \end{bmatrix} = \begin{bmatrix} -\phi_a^{(+)}(x_1) \\ -\phi_b^{(+)}(x_1) \\ 0 \\ 0 \end{bmatrix}, \quad (12)$$

where we have denoted $x_{1,2} = \mp L/2$, r (t) is the reflection (transmission) amplitude assuming the scattering from the left to the right, and A , B are arbitrary complex coefficients associated with linearly-independent solutions $\phi^{(1)}$, $\phi^{(2)}$ of Eqs. (8) and (9) for the central area ($x_1 < x < x_2$). In practice, we take $\phi^{(1,2)}|_{x=x_1} = (1, \pm 1)^T$ and find $\phi^{(1,2)}|_{x=x_2}$ by integrating Eqs. (8) and (9) within a standard forth-order

Runge-Kutta algorithm. (The details of the calculations will be given later.)

Solving Eq. (12), one finds the transmission amplitude t for a given $k_y = k_y^{(n)}$ and $E = \mu$, and the corresponding transmission probability $T_n(\mu) = T_{k_y}(E) = |t|^2$. The supercurrent $I(\theta)$ and the normal-state resistance R_N can then be

determined from Eqs. (6) and (7) by summing over N modes, see Eq. (11).

III. A RECTANGULAR BARRIER AND INFINITELY-DOPED LEADS

For a rectangular barrier of infinite height, corresponding to $m \rightarrow \infty$ and $V_0 \rightarrow \infty$ in Eq. (5), the transmission probability can be written in a compact form [29]

$$T_{k_y}(E) = \left[1 + \left(\frac{k_y}{\varkappa} \right)^2 \sin^2(\varkappa L) \right]^{-1}, \quad (13)$$

with

$$\varkappa = \begin{cases} \sqrt{k_F^2 - k_y^2}, & \text{for } |k_y| \leq k_F, \\ i\sqrt{k_y^2 - k_F^2}, & \text{for } |k_y| > k_F, \end{cases} \quad (14)$$

and the Fermi wavenumber $k_F = |E|/(\hbar v_F)$.

For the Dirac point ($\mu = E = 0$) all transmission probabilities $T_n(\mu) = T_{k_y}(E)$ for $k_y = k_y^{(n)}$ correspond to imaginary \varkappa -s in Eq. (14), indicating the transport via evanescent modes. Additionally, for the wide-sample limit, $W \gg L$, one can approximate the summations in Eqs. (6) and (7) by integrations $0 \leq k_y \leq k_F$, obtaining [16]

$$I(\theta) = \frac{e\Delta_0}{\hbar} \frac{2W}{\pi L} \cos(\theta/2) \operatorname{artanh}[\sin(\theta/2)], \quad (15)$$

and

$$R_N^{-1} = \frac{4e^2}{h} \frac{W}{\pi L}. \quad (16)$$

Finding the maximum of $I(\theta)$ numerically, we get

$$I_c R_N \frac{e}{\Delta_0} = 2.0821 \quad \text{and} \quad S = 0.2548. \quad (17)$$

In the high-doping limit ($|\mu| \gg \hbar v_F/L$), the quantities considered are governed by real \varkappa -s in Eq. (14); however, the argument of sine in Eq. (13) can be regarded as a random phase (φ), the integration over which can be performed independently from the integration over $0 \leq k_y \leq k_F$. In turn,

$$I(\theta) \simeq \frac{e\Delta_0}{\hbar} \frac{W}{\pi} \int_0^{k_F} dk_y \frac{1}{\pi} \int_0^\pi d\varphi \frac{T_{k_y,\varphi} \sin \theta}{\sqrt{1 - T_{k_y,\varphi} \sin^2(\theta/2)}}, \quad (18)$$

where $T_{k_y,\varphi} = \left[1 + \frac{k_y^2}{k_F^2 - k_y^2} \sin^2 \varphi \right]^{-1}$. For the normal-state resistance, the analogous integrations can be performed analytically [22], leading to

$$(T_{k_y})_{\text{approx}} = \frac{1}{\pi} \int_0^\pi d\varphi T_{k_y,\varphi} = \sqrt{1 - (k_y/k_F)^2}, \quad (19)$$

$$R_N^{-1} \simeq \frac{g_0 W}{\pi} \int_0^{k_F} dk_y (T_{k_y})_{\text{approx}} = \frac{\pi}{4} G_{\text{Sharvin}}, \quad (20)$$

with $g_0 = 4e^2/h$ (the conductance quantum for graphene) and the Sharvin conductance $G_{\text{Sharvin}} = g_0 k_F W / \pi = g_0 |\mu| W / (\pi \hbar v_F)$. The prefactor of $\pi/4$ in the last expression of Eq. (20), which was derived for a rectangular sample, justifies the notion of 'sub-Sharvin conductance' and depends only weakly on the system geometry (see Ref. [24]). The numerical optimization for Eq. (18), with respect to θ , leads to

$$I_c R_N \frac{e}{\Delta_0} \simeq 2.4285 \quad \text{and} \quad S = 0.4160. \quad (21)$$

In Fig. 2, we display the current-phase relations given by Eqs. (15) and (18) multiplied by the relevant normal-state resistance, see Eqs. (16) and (20), and by a factor of e/Δ_0 to obtain dimensionless results (thick solid lines). Also in Fig. 2, the two limiting cases for the mesoscopic Josephson equation are illustrated.

The first one is a tunnel junction, with $T_n \ll 1$ for all n , for which one can linearize Eq. (6) in T_n , with the result

$$I(\theta) \simeq \frac{e\Delta_0}{2\hbar} \sum_{n=0}^{N-1} T_n \sin \theta = \frac{\pi\Delta_0}{2e} R_N^{-1} \sin \theta, \quad (22)$$

which is plotted with dashed lines in Fig. 2. In such a limit, we have

$$I_c R_N \frac{e}{\Delta_0} = \frac{\pi}{2} \quad \text{and} \quad S = 0. \quad (23)$$

The second is a perfect ballistic system (or Sharvin contact), for which transmission eigenvalues are equal to either 0 or 1, and can be order such that

$$T_n = \begin{cases} 1, & 0 \leq n < N_0, \\ 0, & N_0 \leq n < N, \end{cases} \quad (24)$$

with the number of open channels $N_0 \ll N$. Substituting the above to Eqs. (6) and (7) we immediately get

$$I(\theta) = N_0 \frac{e\Delta_0}{\hbar} \sin(\theta/2) \operatorname{sgn}(\cos \theta/2), \quad (25)$$

where $\operatorname{sgn}(x)$ is the sign function, and

$$R_N^{-1} = N_0 \frac{4e^2}{h}. \quad (26)$$

In effect, for the ballistic limit

$$I_c R_N \frac{e}{\Delta_0} = \pi \quad \text{and} \quad S = 1. \quad (27)$$

Eq. (25) is visualised in Fig. 2 with thin solid lines.

As can be easily seen from Fig. 2, the graphene-specific current-phase relation differs significantly from the familiar sine function predicted for the tunneling limit, either at the Dirac point ($\mu = 0$) or in the high-doping limit ($|\mu| \gg \hbar v_F/L$); however, it is still far from the relation predicted for the ballistic limit.

The influence of a finite potential step height, as well as the smooth potential shape, is discussed next.

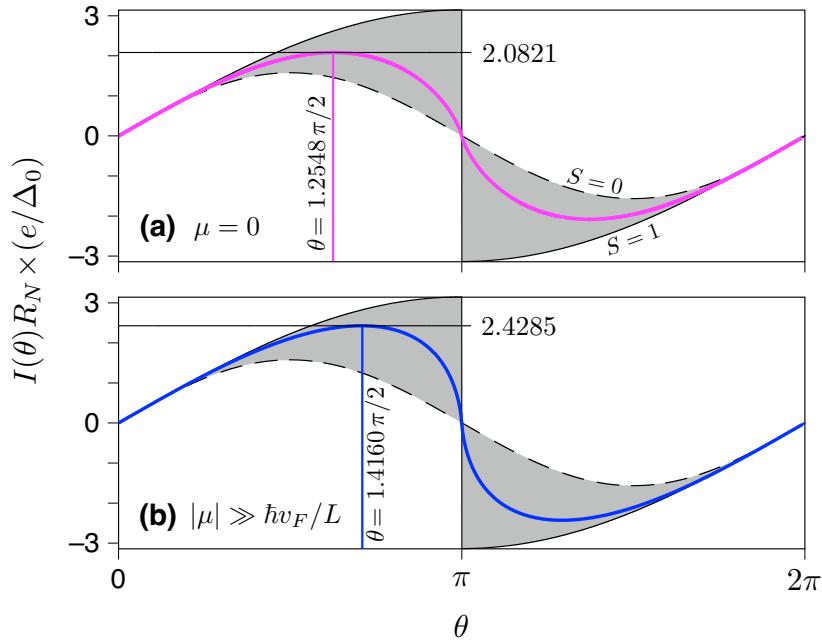


Figure 2: Current-phase relation for S-g-S Josephson junction in the case of rectangular potential barrier and infinitely-doped leads, corresponding to $m \rightarrow \infty$ and $V_0 \rightarrow \infty$ in Eq. (5). (a) The Dirac point ($\mu = 0$), (b) the high-doping limit ($|\mu| \gg \hbar v_F/L$). Results obtained from Eqs. (15) and (18) are displayed with color thick lines. Thin black lines visualize the tunneling limit, see Eq. (22) (dashed lines), and the ballistic limit, see Eq. (25) (solid lines).

IV. SMOOTH POTENTIAL BARRIERS

In this section, we present the central results of the paper, concerning the normal-state conductance $1/R_N$, the critical current I_c , the product $I_c R_N$, and skewness of the current-phase relation for superconductor-graphene-superconductor (S-g-S) Josephson junction depicted in Fig. 1. The numerical calculations are carried out according to Eqs. (5)–(12), for the system with infinite-mass boundary conditions and the width $W = 5L = 1000$ nm. This sets the energy scale that separates the weak- and the high-doping regimes at $\hbar v_F/L = 2.9$ meV. The step height in Eq. (5) is $V_0 = t_0/2 = 1.35$ eV, which yields (for instance) the number of propagating modes in the leads as $N = 691$ for $\mu = -0.1$ eV and $N = 802$ for $\mu = 0.1$ eV. The numerical integration of Eqs. (8) and (9) was performed utilizing a standard fourth-order Runge-Kutta algorithm, with a spacial step of $\Delta x = L/800 = 2.5$ pm. (For each value of k_y , the system analogous to Eq. (12), but describing scattering from the right to the left, was solved independently to find the amplitudes t' and r' , and to check the unitarity of the scattering matrix \mathcal{S} ; the above parameters result in an unitarity error $\epsilon_n = \|\mathcal{S}\mathcal{S}^\dagger - I\| < 10^{-8}$, with $\|A\|$ denoting the maximum absolute value of a matrix element A_{ij} and the identity matrix I , for all cases considered.) Summation over the modes in Eqs. (6), (7) was terminated if $T_n < 10^{-6}$.

The evolution of the conductance spectrum with exponent m in Eq. (5), which was discussed earlier in Ref. [22], is visualized in the top panel of Fig. 3. The bottom panel of Fig. 3 presents a similar evolution of the critical current. Remark-

ably, the behavior of the two physical properties is very similar, particularly in the tripolar regime ($\mu < 0$). For the unipolar regime ($\mu > 0$), I_c decays slightly faster than $1/R_N$ with the increasing m , exhibiting irregular behavior for smaller m -s.

A deeper insight into the system behavior is provided by the evolution of the product $I_c R_N$, as shown in Fig. 4. It is noticeable that the numerical results for smooth potentials and finite V_0 stay close to the *graphene-specific* range, which is defined by the values obtained for the rectangular barrier of an infinite height for $\mu = 0$ and $|\mu| \gg \hbar v_F/L$, see Eqs. (17) and (21), provided that the system is in the tripolar regime ($\mu < 0$). In contrast, in the unipolar regime ($\mu > 0$), $I_c R_N$ evolves — with the increasing m — from the values close to the ballistic limit, see Eq. (27), towards graphene-specific values. (For a ballistic sample, the tunneling limit, see Eq. (23), is not approached.)

The above observations are further supported with the evolution of skewness (S) presented in Fig. 5. Similarly as for $I_c R_N$, the numerical results for all m -s stay within or very close to the graphene-specific range as long as $\mu < 0$. For $\mu > 0$, the evolution from the almost ballistic value towards the higher graphene-specific value is observed as m increases.

Another striking feature of the results presented in Figs. 4 and 5 is that in the vicinity of the Dirac point, $|\mu| \lesssim \hbar v_F/L$, both $I_c R_N$ and S are very close to the values given in Eq. (17) and are almost unaffected by varying m . (For $m = 2$, the minima of $I_c R_N$ and S are shifted towards the tripolar regime, but the minimal values still coincide with the predictions given in Eq. (17).) We emphasize that such robustness is absent for both

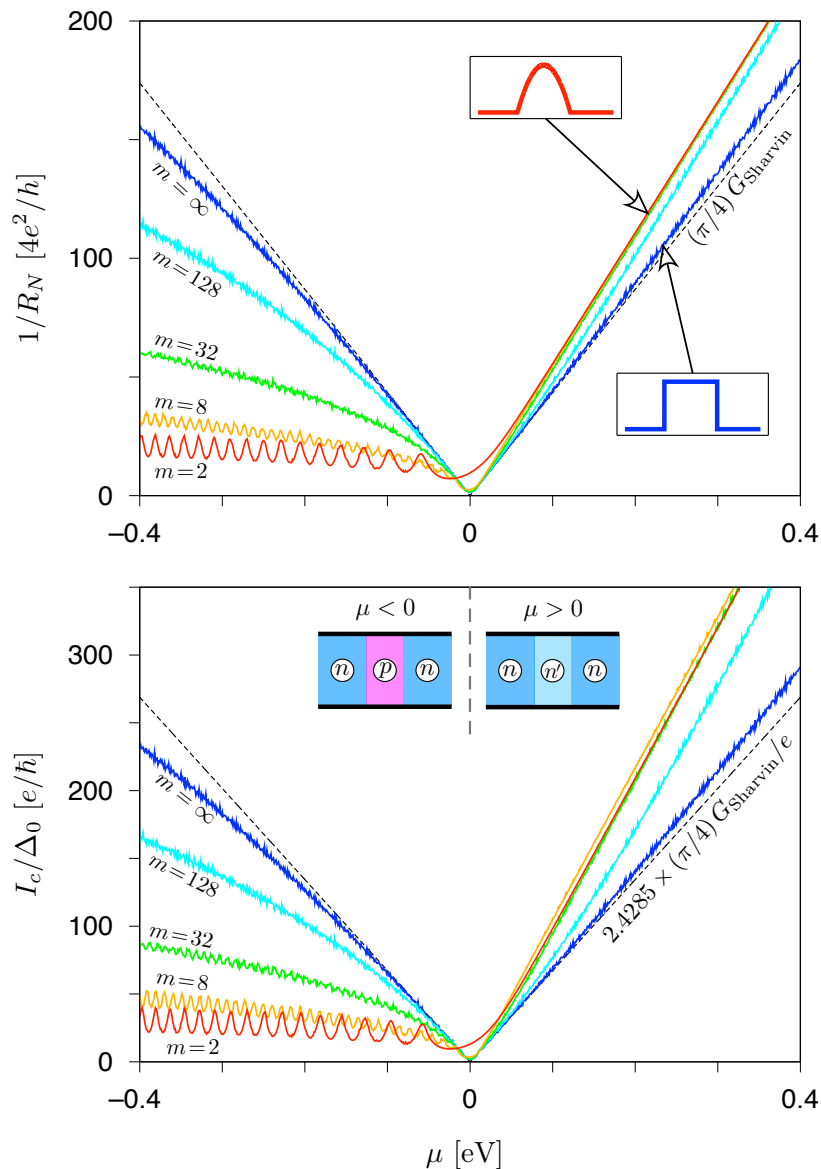


Figure 3: Normal-state conductance $1/R_N$ (top) and critical current I_c (bottom) for the system of Fig. 1 as functions of the chemical potential ($\mu = E$). The parameters are: $W = 5L = 1000$ nm, $V_0 = t_0/2 = 1.35$ eV. The exponent m in Eq. (5) is specified for each dataset (solid lines). Insets (top) depict the potential profiles for $m = 2$ and $m = \infty$. Dashed line depicts the sub-Sharvin conductance given by Eq. (20) and the corresponding critical current, see Eq. (18). (The values of G_{Sharvin} are not shown, as they closely follow the numerical results for $m = 2$ and $\mu > 0$.) Additional insets (bottom) visualize the tripolar (n-p-n) and the unipolar (n-n'-n) doping for $\mu < 0$ and $\mu > 0$ (respectively).

$1/R_N$ and I_c , see Fig. 3. This suggests that intensive quantities, such as the product $I_c R_N$ and skewness S , are better probes of graphene-specific features in S-g-S Josephson junctions. In particular, the S measurement is weakly affected by contact resistances, and the experimental works for S-g-S junctions [18, 19] report values of $S \approx 0.2 \div 0.25$ near the Dirac point as well as in the tripolar regime.

For a somewhat more detailed view of the data we present, in Fig. 6, the product $I_c R_N$ as a function of skewness S for four selected values of μ (since the results near the Dirac point are almost unaffected by changing m , relatively high values of μ were chosen: $\mu = \pm 0.1$ eV, ± 0.2 eV) and nine different

values of m ($m = 2, 4, \dots, 256$, and ∞) for each μ . The two pairs of $(I_c R_N, S)$ defined by Eqs. (17) and (21), bounding the graphene-specific range, are also marked (and indicated with arrows).

To rationalize our numerical results for S-g-S Josephson junction, let us first consider the case of a single nonzero eigenvalue, $0 < T \leq 1$ in Eqs. (6) and (7). Straightforward optimization of $I(\theta)$ with respect to θ leads to the dependence of $I_c R_N$ versus S presented with black solid line in Fig. 6. It is easy to see that the characteristics of such *single-mode Josephson junction* are quite distant from the results for S-g-S junction. For this reason, we put forward a toy model

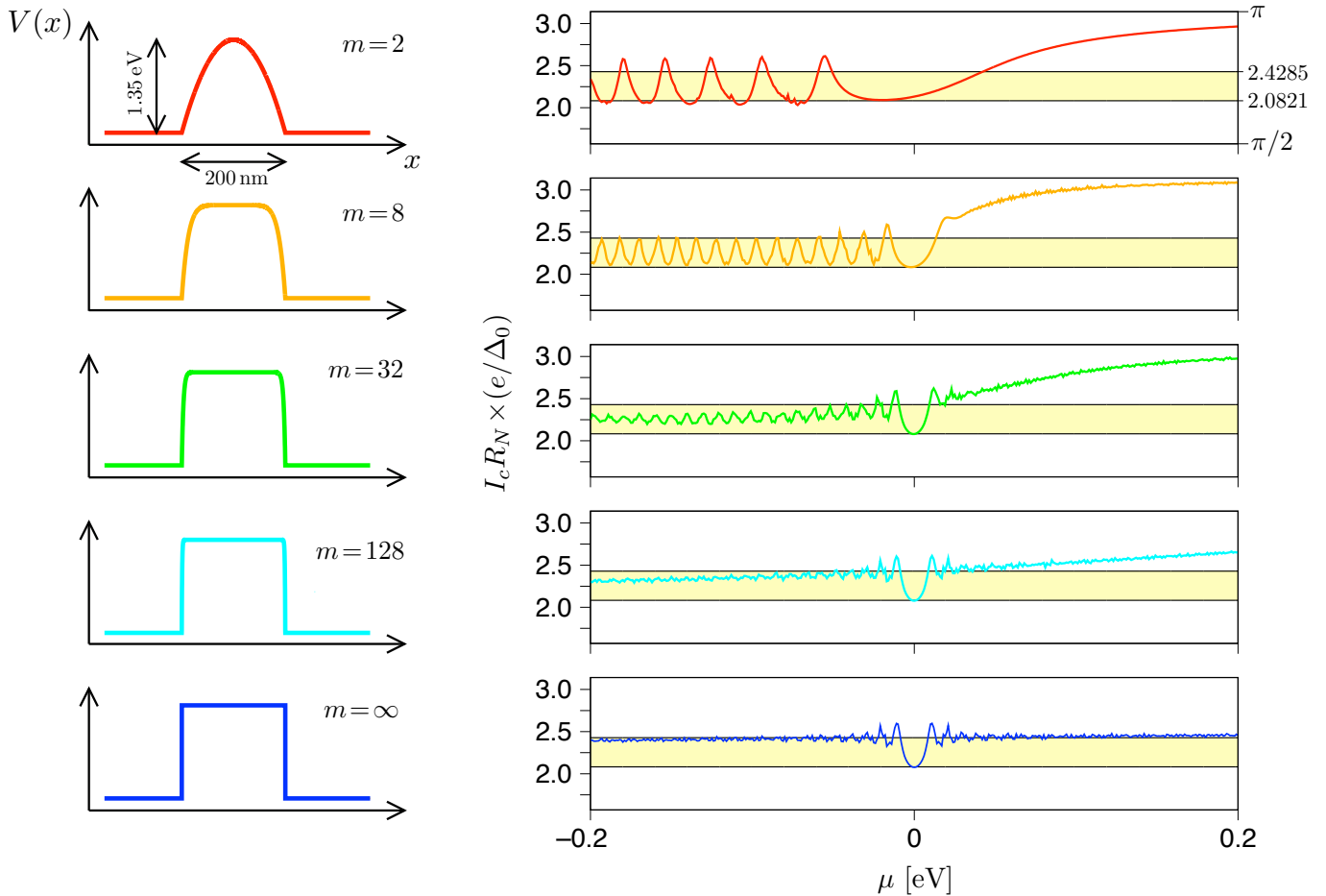


Figure 4: Product $I_c R_N$ for the data shown in Fig. 3. The exponent m in Eq. (5) is varied between the rows. The potential profile for each m is displayed on the left. Horizontal lines bordering the yellow areas on the right mark the values for rectangular barrier of an infinite height ($m \rightarrow \infty$, $V_0 \rightarrow \infty$), corresponding to $\mu = 0$ and $|\mu| \gg \hbar v_F/L$, see Eqs. (17) and (21).

that parametrizes the tunneling-to-ballistic crossover, namely

$$T_{k_y}^{(\Theta)} = \frac{1}{e^{Lk_y - \Theta} + 1} - \frac{1}{e^{Lk_y + \Theta} + 1} \quad (\Theta > 0). \quad (28)$$

It is also supposed that $W \gg L$ and the number of modes in the leads $N \rightarrow \infty$, such that the summations in Eqs. (6) and (7) are replaced by integrations over $0 \leq k_y < \infty$. For instance, $\Theta \rightarrow 0$ reproduces the tunneling limit, with the values of $I_c R_N$ and S given by Eq. (23), whereas $\Theta \gg 1$ corresponds to the ballistic limit. (To be more specific, the value of $I_c R_N$ given in Eq. (27) is reproduced with an accuracy better than 1% for $\Theta \geq 1200$; the same applies for S , starting from $\Theta = 4 \cdot 10^4$.)

The functional dependence of $I_c R_N$ on S , which follows from Eq. (28), is also visualised in Fig. 6 (dotted line). We find that such dependence can be approximated by

$$I_c R_N \frac{e}{\Delta_0} \simeq \frac{\pi}{2}(S+1) + 0.59 S^{0.89} (1-S)^{0.70}. \quad (29)$$

The corresponding curve is omitted since it matches the dotted line in Fig. 6 perfectly.

In contrast to single-mode Josephson junction, the toy-model results stay very close to our S-g-S junction data obtained for $\mu < 0$ and smooth potentials. They also approach the values of $(I_c R_N, S)$ given in Eqs. (17) and (21), with the former being well-reproduced for $\Theta \approx 3.4$, and the latter for $\Theta \approx 6.8$. The data for $\mu > 0$ and smooth potentials are also not far from the toy-model results, staying within the range of

$$\theta_c < I_c R_N \frac{e}{\Delta_0} \lesssim 1.1 \theta_c, \quad (30)$$

with $\theta_c = \pi(S+1)/2$.

V. CONCLUSIONS

We have investigated the basic characteristics of the superconductor-graphene-superconductor (S-g-S) Josephson junction, including the normal-state conductance, critical current, and the skewness of the current phase relation, supposing that the potential profile along the system is tuned from a parabolic to a rectangular shape. Compared to earlier studies of the similar system with a rectangular potential [16, 17],

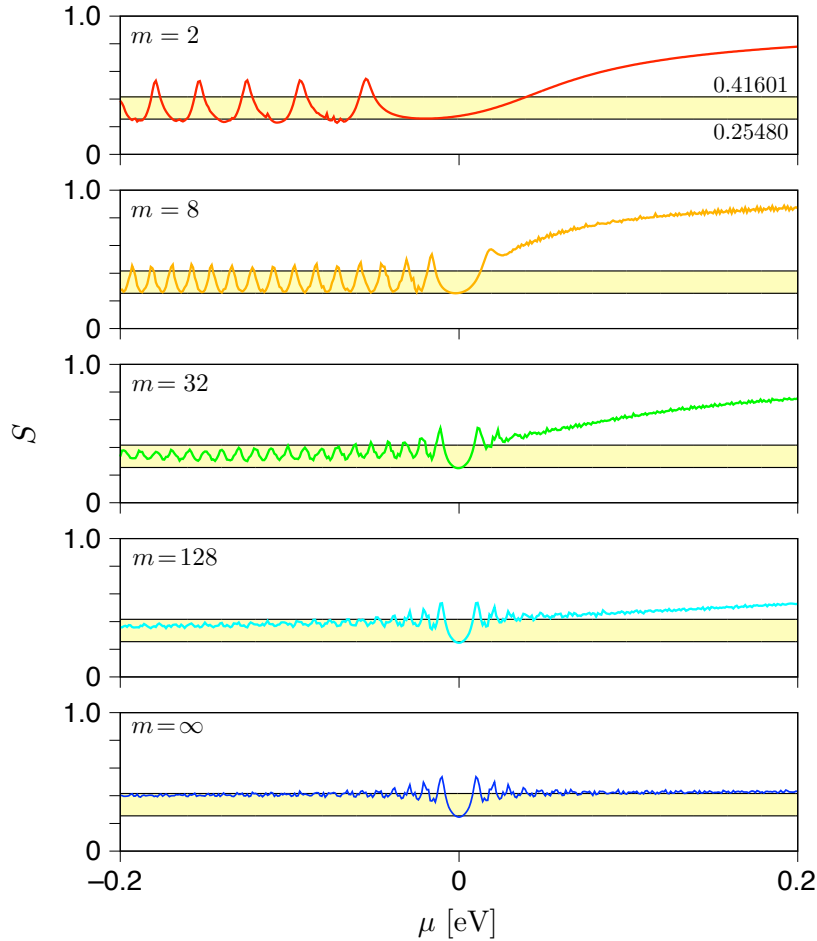


Figure 5: Skewness of the current-phase relation S displayed versus the chemical potential for the same system parameters as in Fig. 3 (solid lines). The exponent m in Eq. (5) is specified for each panel. Horizontal lines mark graphene-specific values of S , see Eqs. (17) and (21).

several new features have been identified: (i) If the doping in the graphene sample close to the Dirac point, the product of critical current and normal-state resistance, as well as the skewness, are very weakly dependent on the potential shape. This is in contrast to the critical current and the normal-state resistance themselves, which show considerable dependence on the potential shape. (ii) In the tripolar regime, where the central part of the sample with hole doping is attached to two regions with electron doping, the aforementioned quantities take on graphene-specific values that are characteristic for an idealized rectangular barrier of infinite height. (iii) In the unipolar regime (electron doping in all parts of the sample) deviations from graphene-specific values are significant and increase when the potential barrier is smoothed.

Therefore, when searching for graphene-specific features in the characteristics of S-g-S Josephson junction, the rectangular potential profile considered in earlier studies is not essential; such features may be observed not only near the Dirac point, but also for relatively high dopings in the tripolar regime.

Moreover, the approximation technique [24] previously used to calculate the conductance and shot-noise power for

a rectangular barrier of infinite height, was adopted for the S-g-S setup to calculate the current-phase relation, improving the approximations for critical current and skewness away from the Dirac point.

We hope that our numerical study — if confirmed experimentally — will extend the list of measurable quantities with graphene-specific values, including the universal conductivity and shot-noise power [30], quantized visible light absorption [31], and the anomalous thermal-to-electric conductivity ratio [32–34].

Acknowledgments

The work was partly completed during a sabbatical granted by the Jagiellonian University in the summer semester of 2024/25. We gratefully acknowledge Polish supercomputing infrastructure PLGrid (HPC Center: ACK Cyfronet AGH) for providing computer facilities and support within computational grant No. PLG/2025/018544.

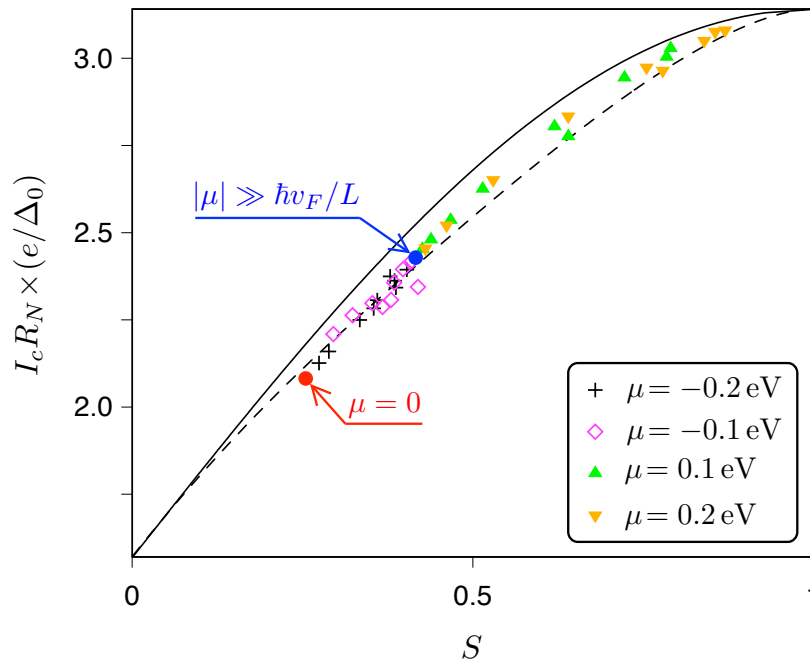


Figure 6: Product $I_c R_N$ displayed versus skewness of the current-phase relation (datapoints). Each dataset contains nine datapoints corresponding to $m = 2, 4, \dots, 256$, and ∞ , for a fixed value of the chemical potential, $\mu = \pm 0.1$ eV, or ± 0.2 eV (see the legend). Remaining system parameters are same as in Fig. 3. Two additional symbols (full circles) mark the values given in Eqs. (17) and (21). Black solid line presents the results following from the optimization of Eq. (6) for a single nonzero eigenvalue $0 < T \leq 1$; black dashed line depicts the results obtained within the toy model defined by Eq. (28).

-
- [1] B. D. Josephson, Possible new effects in superconductive tunnelling, *Phys. Lett.* **1**, 251 (1962).
- [2] P. W. Anderson and J. M. Rowell, Probable Observation of the Josephson Tunnel Effect, *Phys. Rev. Lett.* **10**, 230 (1963).
- [3] B. D. Josephson, Coupled Superconductors, *Rev. Mod. Phys.* **36**, 216 (1964).
- [4] K. K. Likharev, Superconducting weak links, *Rev. Mod. Phys.* **51**, 101 (1979).
- [5] J. M. Martinis, M. H. Devoret, and J. Clarke, Energy-Level Quantization in the Zero-Voltage State of a Current-Biased Josephson Junction, *Phys. Rev. Lett.* **55**, 1543 (1985).
- [6] M. H. Devoret, J. M. Martinis, and J. Clarke, Measurements of Macroscopic Quantum Tunneling out of the Zero-Voltage State of a Current-Biased Josephson Junction, *Phys. Rev. Lett.* **55**, 1908 (1985).
- [7] J. Q. You and F. Nori, Superconducting Circuits and Quantum Information, *Physics Today* **58**, 42 (2005).
- [8] G. Wendin, Quantum information processing with superconducting circuits: a review, *Rep. Prog. Phys.* **80** 106001 (2017).
- [9] M. Tinkham, *Introduction to Superconductivity*, (Dover, New York, 2004).
- [10] T. Akazaki, J. Nitta, H. Takayanagi, T. Enoki, and K. Arai, Improving the mobility of an $\text{In}_{0.52}\text{Al}_{0.48}\text{As}/\text{In}_{0.53}\text{Ga}_{0.47}\text{As}$ inverted modulation-doped structure by inserting a strained InAs, *Appl. Phys. Lett.* **65**, 1263 (1994).
- [11] A. F. Morpurgo, T. M. Klapwijk, and B. J. van Wees, Hot electron tunable supercurrent, *Appl. Phys. Lett.* **72**, 966 (1998).
- [12] H. Heersche, P. Jarillo-Herrero, J. Oostinga, L. M. K. Vandersypen, and A. F. Morpurgo, Bipolar supercurrent in graphene, *Nature* **446**, 56 (2007).
- [13] G. De Simoni, F. Paolucci, C. Puglia, and F. Giazotto, Josephson field-effect transistors based on all-metallic Al/Cu/Al proximity nanojunctions, *ACS Nano* **13**, 7871 (2019).
- [14] I. Golokolenov, A. Guthrie, S. Kafanov, Yu. A. Pashkin, and V. Tsepelin, On the origin of the controversial electrostatic field effect in superconductors, *Nat. Commun.* **12**, 2747 (2021).
- [15] C. W. J. Beenakker, Three "universal" mesoscopic Josephson effects, in *Transport Phenomena in Mesoscopic Systems*, edited by H. Fukuyama and T. Ando (Springer, Berlin, 1992). doi:10.1007/978-3-642-84818-6_22.
- [16] M. Titov and C. W. J. Beenakker, Josephson effect in ballistic graphene, *Phys. Rev. B* **74**, 041401(R) (2006).
- [17] A. G. Moghaddam and M. Zareyan, Josephson effect in mesoscopic graphene strips with finite width, *Phys. Rev. B* **74**, 241403(R) (2006).
- [18] C. D. English, D. R. Hamilton, C. Chialvo, I. C. Moraru, N. Mason, and D. J. Van Harlingen, Observation of nonsinusoidal current-phase relation in graphene Josephson junctions, *Phys. Rev. B* **94**, 115435 (2016).
- [19] G. Nanda, J. L. Aguilera-Servin, P. Rakytka, A. Kormányos, R. Kleiner, D. Koelle, K. Watanabe, T. Taniguchi, L. M. K. Vandersypen, S. Goswami, Current-Phase Relation of Ballistic Graphene Josephson Junctions, *Nano Lett.* **17**, 3396 (2017).
- [20] V. Ambegaokar and A. Baratoff, Tunneling Between Superconductors, *Phys. Rev. Lett.* **10**, 486 (1963); *ibid.* **11**, 104(E) (1963).
- [21] I. O. Kulik and A. N. Omel'yanchuk, Contribution to the microscopic theory of the Josephson effect in superconducting

- bridges, *Pis'ma Zh. Eksp. Teor. Fiz.* **21**, 216 (1975) [*Sov. Phys. JETP Lett.* **21**, 96 (1975)]. Available online: http://jetpletters.ru/ps/0/article_22289.shtml.
- [22] A. Rycerz and P. Witkowski, Sub-Sharvin conductance and enhanced shot noise in doped graphene, *Phys. Rev. B* **104**, 165413 (2021).
- [23] A. Rycerz, Wiedemann–Franz law for massless Dirac fermions with implications for graphene, *Materials* **14**, 2704 (2021).
- [24] A. Rycerz, The Quantum Transport of Dirac Fermions in Selected Graphene Nanosystems Away from the Charge Neutrality Point, *Materials* **18**, 2036 (2025).
- [25] M. Acciai, L. Arrachea, and J. Splettstoesser, Quantum transport phenomena induced by time-dependent fields, *Riv. Nuovo Cimento* **48**, 653 (2025).
- [26] C. W. J. Beenakker, Specular Andreev Reflection in Graphene, *Phys. Rev. Lett.* **97**, 067007 (2006).
- [27] M. V. Berry and R. J. Mondragon, Neutrino billiards: time-reversal symmetry-breaking without magnetic fields, *Proc. R. Soc. Lond. A* **412**, 53 (1987).
- [28] M. Büttiker, Y. Imry, R. Landauer, and S. Pinhas, Generalized many-channel conductance formula with application to small rings, *Phys. Rev. B* **31**, 6207 (1985).
- [29] A. Rycerz, P. Recher, and M. Wimmer, Conformal mapping and shot noise in graphene, *Phys. Rev. B* **80**, 125417 (2009).
- [30] M. I. Katsnelson, *The Physics of Graphene*, 2nd ed. (Cambridge University Press, Cambridge, UK, 2020); Chapter 3.
- [31] R. R. Nair, P. Blake, A. N. Grigorenko, K. S. Novoselov, T. J. Booth, T. Stauber, N. M. R. Peres, and A. K. Geim, Fine Structure Constant Defines Visual Transparency of Graphene, *Science* **320**, 1308 (2008).
- [32] J. Crossno, J. K. Shi, K. Wang, X. Liu, A. Harzheim, A. Lucas, S. Sachdev, P. Kim, T. Taniguchi, K. Watanabe, T. A. Ohki, and K. C. Fong, Observation of the Dirac fluid and the breakdown of the Wiedemann-Franz law in graphene, *Science* **351**, 1058 (2016).
- [33] D. Suszalski, G. Rut, and A. Rycerz, Lifshitz transition and thermoelectric properties of bilayer graphene, *Phys. Rev. B* **97**, 125403 (2018).
- [34] Y.-T. Tu and S. Das Sarma, Wiedemann-Franz law in graphene, *Phys. Rev. B* **107**, 085401 (2023).